

Dispersive wave generation in photonic crystal fibers with normal dispersion pumping

E. CREVON, C. KHALLOUF, J. M. DUDLEY, AND T. SYLVESTRE*

¹Institut FEMTO-ST, CNRS-Université de Franche-Comté, 25030 Besançon, France

*thibaut.sylvestre@univ-fcomte.fr

Compiled March 31, 2025

We present a comprehensive numerical and experimental investigation of dispersive wave emission in photonic crystal fibers, generated from femtosecond pulses under normal dispersion pumping. Particular attention is given to the roles of self-phase modulation and optical wave breaking in shaping both the temporal and spectral characteristics of the pulses in the presence of higher-order dispersion. Our findings underscore the critical importance of accounting for higher-order dispersion to accurately model the dynamics of optical wave breaking and dispersive wave generation in the anomalous dispersion regime. Experimentally, our results show excellent agreement with numerical simulations, further validating the model. Additionally, we examine polarization effects and supercontinuum relative intensity noise using the dispersive Fourier transform technique.

1. INTRODUCTION

Supercontinuum (SC) laser sources based on photonic crystal fibers (PCFs) have gained significant attention in recent years, driving advancements in both scientific research and practical applications [1, 2]. A crucial factor behind the success of PCFs for SC generation is the ability to align the fiber's zero-dispersion wavelength (ZDW) with the operational wavelength of ultrafast laser systems, allowing for efficient excitation of soliton dynamics that underpin spectral broadening. To trigger soliton dynamics, short pulses are launched into the fiber's weak anomalous dispersion regime, where the pulse undergoes higher-order soliton compression and subsequently breaks into fundamental solitons. These solitons are then influenced by higher-order dispersion effects and stimulated Raman scattering (SRS), resulting in the emission of dispersive waves (DW) toward the visible in the normal dispersion regime, and the soliton self-frequency shift (SSFS) toward the infrared [3]. The generation of DWs from solitons, also known as resonant or Cherenkov-like radiations, has been thoroughly studied in photonic crystal fibers with various dispersion and phase-matching conditions [3–7].

However, recent studies have expanded the understanding of DW emission, revealing that it is not limited only to soliton pulses in the anomalous dispersion regime [8–11]. In particular, it has been shown that power

transfer from a pump in the normal dispersion regime to a DW in the anomalous dispersion regime can also occur due to the third-order dispersion [8]. This concept has been even theoretically extended to account for fourth-order dispersion, further demonstrating the potential to generate multiple DWs from normal dispersion pumping [10]. In both cases, the frequency shift of the DW is determined by phase-matching conditions. This shift is influenced not only by dispersion but also by self-phase modulation (SPM) and optical wave breaking (OWB), the two key nonlinear effects that tend to dominate propagation in the normal dispersion regime [10].

In this paper, we present a detailed numerical and experimental investigation of dispersive wave (DW) emission from femtosecond pulses propagating in the weak normal dispersion regime of a polarization-maintaining (PM) photonic crystal fiber. We begin by introducing the DW generation process through numerical simulations based on the generalized nonlinear Schrödinger equation (GNLSE). Next, we examine the impact of third-order dispersion on SPM and OWB, with a particular focus on DW emission in the anomalous regime, analogous to soliton-induced DWs in the normal dispersion. However, in this case, the DW frequency detuning follows a different phase-matching condition compared to the soliton regime, as it must also account for the pump frequency chirp

induced by SPM [8]. We compare this phase-matching method with the results of numerical simulations. We then provide experimental results on supercontinuum (SC) generation in the PM-PCF, involving SPM, OWB, and DW emission, by tuning the pump wavelength and peak power. Our experimental findings show strong agreement with GNLSE-based simulations and the phase-matching equation. Furthermore, we explore the transitional dynamics between the normal and anomalous dispersion regimes and investigate the role of polarization effects. We also assess SC noise and stability using the dispersive Fourier transform (DFT) technique. The results underscore the critical role of higher-order dispersion in accurately modeling SC generation when pumping in the normal dispersion regime.

2. NUMERICAL MODEL

Understanding SC generation, particularly the generation of DW in the anomalous dispersion domain, involves observing nonlinear phenomena during the propagation of ultrashort femtosecond laser pulses in nonlinear media such as optical fibers. To achieve this, reliable and comprehensive numerical modeling of nonlinear pulse propagation in dispersive media is essential. Our approach employs the generalized nonlinear Schrödinger equation [3], as described in equation 1. This equation is fundamental for simulating the complex interactions and effects observed in SC generation. It can be expressed in the following form:

$$\frac{\partial A}{\partial z} + \frac{\alpha}{2}A - \sum_{k \geq 2} \frac{i^{k+1}}{k!} \beta_k \frac{\partial^k A}{\partial T^k} = i\gamma(1 + i\tau_s \frac{\partial}{\partial T}) \times \left(A(z, T) \int_{-\infty}^{\infty} R(T') |A(z, T - T')|^2 dT' \right) \quad (1)$$

Where $A(z, T)$ is the complex amplitude of the electrical field normalized such as $|A(z, T)|^2$ gives the instantaneous power in watts. Equation 1 showcases both linear propagation (left-hand side) and nonlinear propagation effects (right-hand side). The coefficients α and β_k represent, respectively, the linear loss and Taylor series expansion of the group velocity dispersion around a central angular frequency (input pulse angular frequency ω_0). The coefficients γ , τ_s and $R(T)$ are respectively the nonlinear coefficient, the self-steepening characteristic time (related to shock formation), and the nonlinear Raman response [4, 12] defined as follows:

$$\gamma = \frac{\omega_0 n_2}{c A_{eff}}, \quad \tau_s = \frac{1}{\omega_0}, \quad R(T) = (1 - f_R)\delta(T) + f_R h_R(T) \quad (2)$$

Where n_2 is the nonlinear index of silica glass assumed to be frequency-independent. n_2 is typically $2.6 \times 10^{-20} \text{ m}^2/\text{W}$ for silica-based fibers for wavelengths around 1000 nm [4]. f_R is the Raman fractional contribution to the Kerr effect and is typically 0.18 for fused silica [4]. h_R is

defined such as to have $\int_0^{\infty} h_R(T) dT = 1$. A_{eff} is the fundamental mode effective area. Equation 1 is numerically solved using the split-step Fourier method with Matlab.

A. Normal dispersion pumping

This study focuses on femtosecond SC generation in the ND regime, where the underlying mechanisms differ significantly from those in the solitonic regime. In ND fibers, SC generation is primarily driven by coherent effects such as SPM and OWB [13–15]. While SPM is well-known to dominate the initial evolution, OWB plays a crucial role in significantly broadening the spectrum beyond the limits of SPM via four-wave mixing (FWM), thus extending the initially narrow SPM spectrum [13, 16]. In the time domain, OWB manifests as a dispersive shock wave (DSW), characterized by damped oscillations in the pulse wings. These oscillations result from the interference between the SPM-generated chirp sidebands and the linear parts of the pulse [17–19]. This nonlinear pulse propagation in the ND regime is numerically illustrated in Figs. 1.

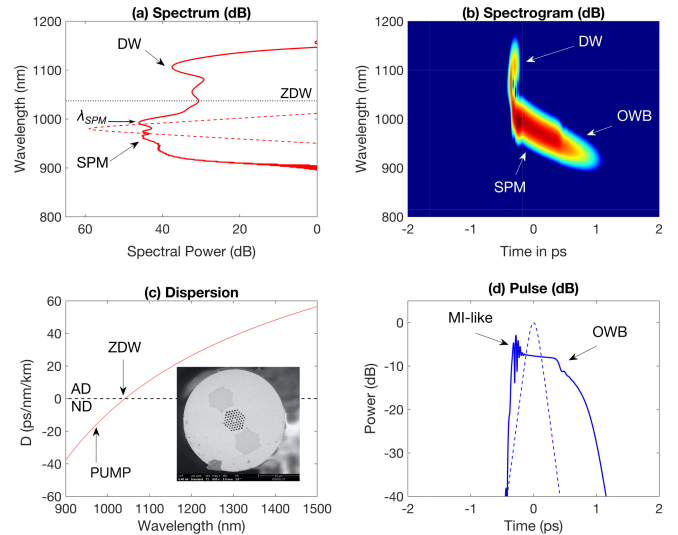


Fig. 1. (a) Fiber input (dashed) and output (solid) pulse spectra, showing SC generation under normal dispersion pumping and DW emission at 1130 nm. (b) Time-frequency spectrogram showing DW emission driven by SPM in the anomalous dispersion (AD) region. (c) Group-velocity dispersion D of the experimentally used PCF, with the ZDW at 1042 nm and the pump wavelength at 980 nm in the normal dispersion (ND) regime. The inset shows the cross-section of the PCF under test. (d) Fiber input (dashed) and output (solid) pulse profiles. The input conditions are a 140 fs (FWHM) Gaussian pulse at 980 nm with a peak power of $P=7$ kW, and a propagation distance of 80 cm.

Here, we specifically examine the influence of higher-order dispersion at wavelengths below the ZDW and explore its impact on the broadening and evolution of both the pulse profile and its spectrum. We numerically investi-

gate this scenario using an initial Gaussian pulse of 140 fs duration (FWHM) at a wavelength of $\lambda_p=980$ nm, with a peak power of $P=7$ kW, propagating through an 80 cm long polarization-maintaining PCF (NKT Photonics SC-5-1040-PM). The PCF cross-section is shown in the inset of Fig. 1 (c), and the computed dispersion curve, plotted as a red line, reveals a ZDW at 1042 nm.

Figure 1(b) provides a spectrogram analysis of the output pulse from the fiber, while Figs. 1(a) and (d) show the input and output spectra and pulses on a logarithmic scale, respectively. The results in Figure 1 highlight the generation of a DW near 1130 nm, an example of the generalized DW generation with ND pumping discussed in Ref. [8]. The phenomenon of OWB is also clearly visible in the spectrogram, manifesting in both the temporal and spectral domains.

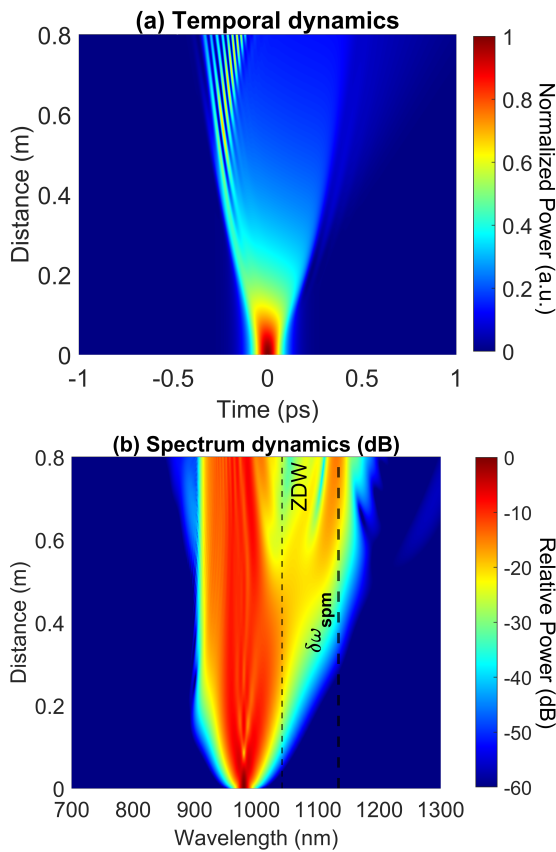


Fig. 2. Numerical simulations: Temporal (a) and spectral (b) evolution along the PCF fiber, showing the DW generation at 1130 nm and the interferences in the time domain, using the same parameters as in Fig.1. a) Time evolution with Δk_1 estimation (white dashed line). b) Direct comparison of DW model $\delta\omega_{spm}$ (black dashed line) with numerical simulations.

As strong modulations develop in the time domain (Figure 1d), corresponding oscillations are observed in the spectrogram, accompanied by DW emitted simultaneously. This superposition of radiation in the spectral domain at specific moments in the temporal domain leads

to oscillations on the top left of the pulse, similar to the effect of modulation instability (MI). We note that the simulated pulse profile shown in Fig. 1(d) has already been observed experimentally using the frequency-resolved optical gating technique [20]. The oscillations observed in the spectrogram (Figure 1(b)) are closely linked to SPM, as reflected in the spectral domain (Figure 1(a)). Whether the emitted DW originates from SPM in the spectral domain or MI-like oscillations in the temporal domain, it contributes to the formation of a DW. These phenomena are more likely to occur near the ZDW, as illustrated by the dispersion curve in Figure 1(c). This underlines the reason for selecting a pump wavelength of $\lambda_p=980$ nm for this study. Future research will investigate alternative pump wavelengths to further explore their impact on DW generation.

To gain deeper insights into the nonlinear dynamics, we plot in Figs. 2 (a) and (b) the temporal and spectral evolution of the femtosecond pulse along the fiber. In the time domain, the pulse undergoes significant broadening due to normal dispersion, while in the spectral domain, we observe clear spectral broadening and the generation of a DW as the pulse spectrum crosses the ZDW barrier, indicated by the dashed black line in Fig.2 (b). In the time domain, strong intensity modulations are present on the pulse (top left), with the suppression of OWB on the trailing edge of the pulse. It is important to emphasize that the observed behaviors in Fig. 1 and Fig.2 contrast with those reported in Ref. [8] for the picosecond regime, where OWB and MI-like oscillations were not observed. Furthermore, in our case, stimulated Raman scattering (SRS) is negligible due to the significant DW frequency detuning (40 THz), which far exceeds the Raman frequency shift (13.5 THz). However, the effect of self-steepening is not negligible in the femtosecond regime, as it induces a slight shift (a few nm) in the DW frequency detuning (not shown here).

B. Phase-matching

Similar to DWs emitted by solitons with anomalous dispersion pumping, there is also a phase-matching condition that allows the prediction of the DW frequency for the case of normal dispersion pumping. To accurately determine the frequency shift of the DW emitted in the anomalous regime, it is crucial to use a reliable phase-matching model. In this study, we will use the method from Ref. [8]. The method to compute the position of the DW considers that DW generation in the anomalous regime is driven by SPM, as shown by the spectrogram in Fig. 1(b). Consequently, the wavelength at which the DW is generated, λ_{DW} , is linked to the SPM-induced positive chirp at a wavelength close to the ZDW, λ_{SPM} , rather than at the pump wavelength itself, λ_p [8, 9]. λ_{SPM} is indicated as an arrow in Fig. 1(a). This shift in wavelength necessitates calculating the second and third-order dispersion coefficients at the λ_{SPM} rather than at the λ_p , as is typically done in the soliton regime. The generation of the

DW in the anomalous domain is therefore governed by a modified equation 3, which does not include any additional nonlinear terms. This adjustment is accounted for by the nonlinear phase shift and the SPM-induced frequency chirp. In angular frequency unit, this equation can be readily written as [8]

$$\delta\omega_{spm} = \frac{-3\beta_2(\omega_{spm})}{\beta_3(\omega_{spm})} \quad (3)$$

Figure 2 (b) compares the model for predicting DW position in wavelength, using Eq.3 with numerical simulations. This value is compared against the spectrum evolution simulated by the GNLSE for a pump wavelength of $\lambda_p = 980$ nm and a power of $P = 7$ kW. The results in Figure 2 (b) confirm the reliability of using $\delta\omega_{spm}$ for predicting the DW position. However, it is important to highlight that the wavelength at which SPM occurs has been determined numerically through spectrogram analysis, which is highly sensitive to different parameters.

B.1. Comparison between theory and simulation

By applying Eq.3 to calculate the position of the dispersive wave, we can compare their predictions with the results obtained from the GNLSE simulations. Figure 3 (a) illustrates the evolution of the DW position in wavelength, alongside the simulated DW, as a function of peak power at a pump wavelength of $\lambda_p = 980$ nm. Similarly, Figure 3 (b) compares the same behaviors with an input peak power at $P = 10$ kW as a function of pump wavelength.

The results in Figure 3 demonstrate that the prediction derived from the theoretical formula based on the SPM wavelength ($\delta\omega_{spm}$), are close to those obtained numerically, which strongly supports the method introduced in Ref. [8]. On the other hand, the values predicted by the relation in Eq. 3 show good agreement with the simulated results, underscoring the reliability of this approach. The next phase of this study will involve comparing the numerically obtained values with experimental data to further validate the method.

3. EXPERIMENTAL MEASUREMENTS

A. Experimental setup

The objective of the experiment is to investigate DW generation under normal dispersion pumping. The experimental setup, illustrated in Figure 4, utilizes a high-power, femtosecond mode-locked Ti:Sa pump laser (Coherent Chameleon). This laser delivers 140 fs Gaussian pulses, tunable over a wavelength range from 680 nm to 1080 nm, with a repetition rate of 80 MHz and a maximum average power of 3.8 W at 800 nm.

To analyze the polarization dependence of the spectrum, a half-wave plate (HWP) is introduced, while a variable density filter (VDF) is used to control and examine the effects of varying power levels. The pulses are then coupled into the microstructured optical fiber (NKT Photonics; Model: SC-5.0-1040-PM), and the output spectrum

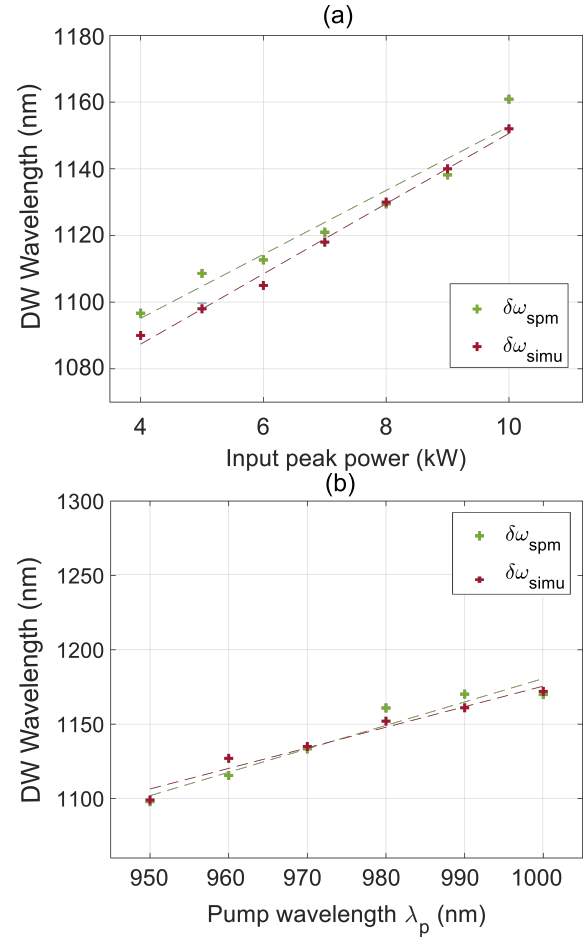


Fig. 3. Evolution of the dispersive wave wavelength according to the analytical method $\delta\omega_{spm}$ (green) with the positions obtained by the simulation $\delta\omega_{simu}$ (red) for different peak power with a pump wavelength a) $\lambda_p = 980$ nm and b) for different pump wavelength at input peak power $P = 10$ kW.

is recorded using an optical spectrum analyzer (OSA). The fiber has a length of $L = 80$ cm.

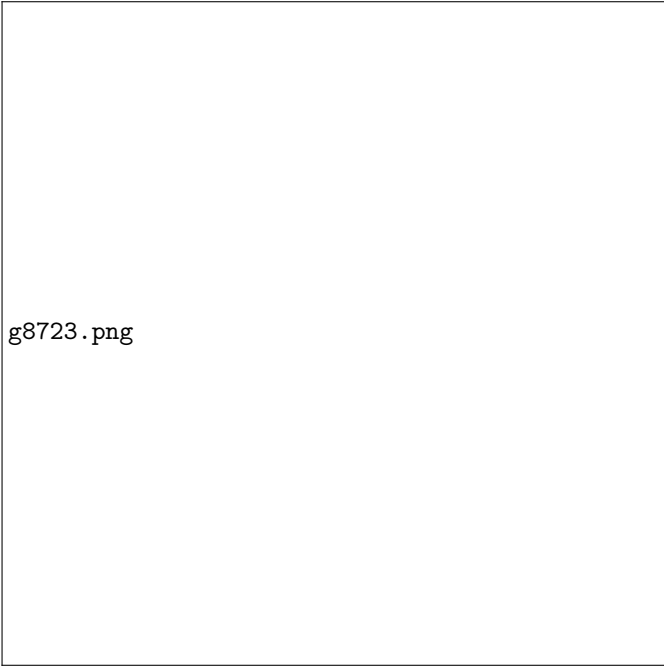


Fig. 4. Scheme of the experimental setup including a tunable femtosecond Ti:Sa laser, a half-wave plate (HWP), a variable density filter (VDF), a 40X microscope objective, the photonic crystal fiber under study, and an optical spectrum analyzer (OSA). The DFT port includes a DCF fiber, a 25-GHz photodiode, and a real-time 20 GHz oscilloscope.

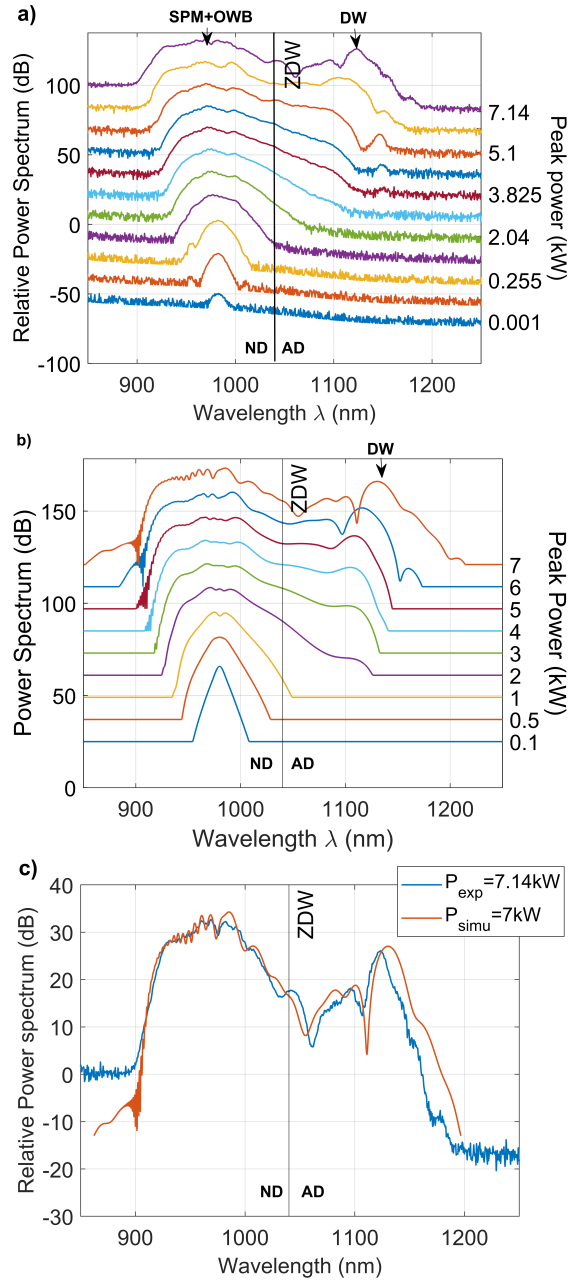


Fig. 5. (a) Experimental and (b) numerical output spectra as a function of input peak power, showing the progressive generation of a dispersive wave near 1130 nm in the anomalous dispersion for a pump wavelength $\lambda_p=980$ nm. All spectra are vertically shifted for improved clarity. (c) Direct comparison of the experimental and numerical spectra for peak powers $P_{exp}=7.14$ kW and $P_{simu}=7$ kW.

A.1. Measurements at $\lambda_p = 980$ nm for different output powers

We next examined the SC spectrum for a fixed pump wavelength of $\lambda_p = 980$ nm, varying the power to observe the different stages of the OWB process. Our goal was to track the emergence of the DW during propagation, as illustrated in Fig. 5 (a). As the SC spectrum evolves, we observe that as the spectrum begins to broaden, it

To control and monitor the power launched into the PCF core, we use a power meter (PWM). The measured power is an average value, reaching up to $P_{in}=280$ mW to prevent any damage of the fiber input face. The results are presented in terms of peak power and pumping wavelength to ensure consistency with the simulations.

becomes increasingly asymmetrical towards the longer wavelengths, influenced by the third-order dispersion coefficient, β_3 . Additionally, on the shorter wavelength side, the spectrum exhibits self-steepening, a result of the OWB phenomenon. At higher power levels, a DW is generated at 1130 nm in the anomalous dispersion region, shifting towards longer wavelengths as the power increases. This shift aligns with the fact that the pump frequency chirp increases with power, resulting in phase-matching being achieved at longer wavelengths for DW.

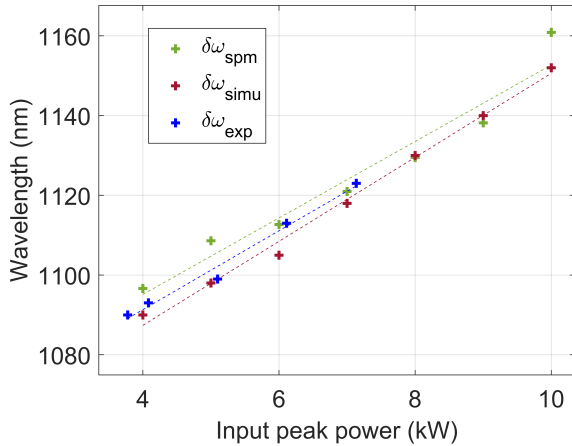


Fig. 6. Evolution of the position of the dispersive wave according to the phase-matching $\delta\omega_{spm}$ (green), the simulation $\delta\omega_{simu}$ (red), and the experiment $\delta\omega_{exp}$ (blue) for different input peak power with a pump wavelength $\lambda_p = 980$ nm.

A.2. Comparison between simulations and experiments

The experimental measurements aim to validate the theoretical or numerical predictions made earlier. To verify the accuracy of the numerical simulations against the experimental results, we focus on comparing the power evolution in Figure 5 (a) for $\lambda_p = 980$ nm with the corresponding power evolution obtained from numerical simulations. The agreement between the experimental and simulated results is very good, particularly at lower wavelengths where the SPM oscillations are almost identically represented, albeit with a slight shift in the DW frequency. This discrepancy between the simulated and experimental spectra stems from the need to further optimize the simulated spectrum to achieve perfect alignment with the experimental data. However, optimizing the spectrum is challenging since it already closely matches the SPM generation, and even small power adjustments do not lead to a significantly better fit. Nonetheless, given the overall consistency between the numerical and experimental results, we can conclude that the methods for predicting the position of the DW, as detailed in Figure 3, can be applied to the experiment.

A.3. Measurements for different pump wavelengths

This initial experiment investigates the evolution of the SC spectrum across different wavelengths to highlight the transition from the normal to the anomalous dispersion region. The selected pump wavelengths range from $\lambda = 910$ nm to $\lambda = 1080$ nm, with the ZDW at $\lambda_{ZDW} = 1042$ nm. As the wavelength increases, the initial power of $P = 17.1$ kW gradually decreases to 3.4 kW, following the laser's power curve. Figure 7 illustrates the output pulse spectra across this wavelength range, emphasizing the effect of pump wavelength on the DW position.

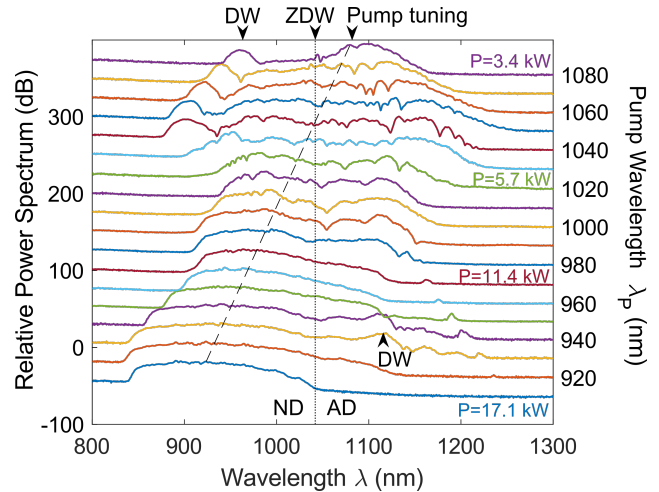


Fig. 7. Experimental Results: Evolution of the fiber's output SC spectrum as a function of the pump wavelength around the zero-dispersion wavelength and for different input peak powers from $P = 17.1$ kW to 3.4 kW, following the laser's power curve. All spectra are vertically shifted for improved clarity.

This result demonstrates the evolution of the DW generated in both the dispersion regimes. Additionally, it highlights the transition between these two regimes. When pumping occurs in the ND regime, the dispersive wave is generated in the anomalous regime, and conversely, it is generated in the normal regime when pumping occurs in the anomalous (soliton) regime. This transition is significant because, in the anomalous region, the generation of the dispersive wave is a direct consequence of the radiation emitted during soliton formation. In the normal region, however, the dispersive wave is essentially shed by SPM. Another important point is that the power threshold for DW generation differs significantly between the two dispersion regimes. This difference explains the sharp reduction in peak power, which drops from 17.1 kW to just 3.4 W. In the anomalous dispersion regime, soliton pulse compression leads to a lower threshold for DW generation, while in the normal dispersion regime, pulse broadening occurs, requiring a much higher threshold.

B. Polarization analysis

To investigate the polarization properties of the SC spectrum and assess the polarization-maintaining performance of the PCF, we examined how input polarization influences its dynamics. This was achieved by rotating the half-wave plate in the experimental setup (Figure 4), while keeping both the pump wavelength and output power constant. By doing so, we could verify whether the fiber effectively maintains polarization and facilitates DW generation. The results, shown in Figure 8(a) and (b) for two pump wavelengths $\lambda_p=970$ nm and $\lambda_p=1000$ nm, clearly demonstrate the impact of the input polarization angle on spectral broadening and the emergence of four-wave mixing (FWM) peaks.

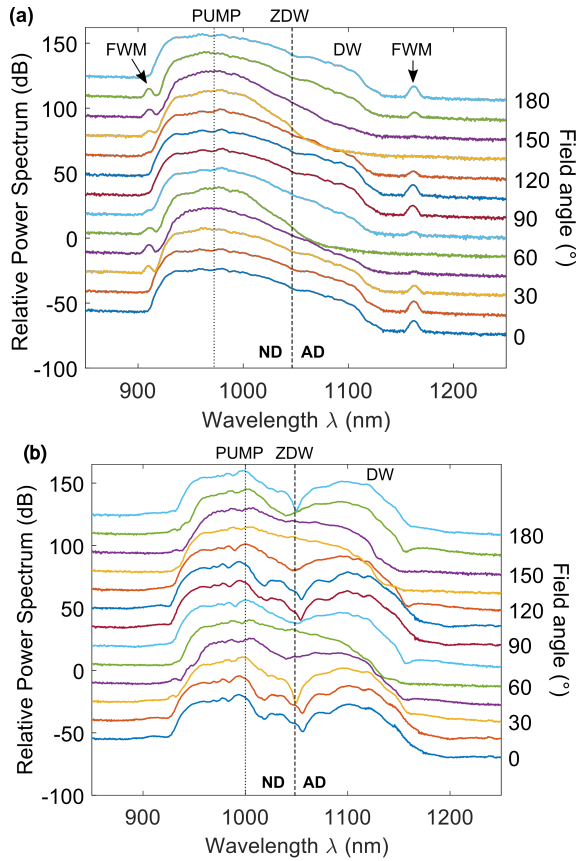


Fig. 8. Experimental spectra as a function of the polarization angle of the input field, for (a) a pump wavelength $\lambda_p=970$ nm and a peak power of $P=3.5$ kW and (b) a pump wavelength $\lambda_p=1000$ nm and a peak power of so $P=3$ kW. 0° angle corresponds to the field aligned with one of the principal axes of the fiber. All spectra are vertically shifted for improved clarity.

When varying the polarization angle, Fig. 8 reveals a periodicity of approximately 90° , corresponding to the slow and fast axes of the PCF. At a pump wavelength of $\lambda_p = 970$ nm, when the polarization is off-axis (around 60°), the SC spectrum exhibits reduced broadening due to polarization mode dispersion and degenerate cross-phase modulation (XPM). Moreover, the FWM peaks are

highly sensitive to polarization: near the principal axes, the peaks are prominent and distinct, while off-axis, they shift to the opposite side of the spectrum. Similarly, at $\lambda_p = 1000$ nm, the spectrum shows less broadening under these conditions. Interestingly, when the field is aligned along one of the principal axes (0° , 90° , or 180°), the spectrum displays a dip near the zero-dispersion wavelength, with no FWM sidebands observed at this pump wavelength.

C. Dispersive Fourier Transform (DFT)

We also conducted SC stability analysis using the DFT technique to assess the impact of DW generation, as depicted in Fig. 4. This method enables real-time, pulse-to-pulse SC spectra recording in the time domain using a time-stretched technique based on normally dispersive dispersion-shifted fiber (DSF) [21, 22]. Due to the quadratic second-order dispersion, the stretched pulses acquire output temporal profiles that mirror the shape of the input pulse spectrum. The experimental setup is shown in Fig. 4. Specifically, to stretch the SC pulses, we added a 440-meter-long DSF at the PCF's output and we then recorded the 80 MHz stretched pulse train using a high-speed, photodiode (Newfocus - 25 GHz) paired with a 20 GHz real-time oscilloscope (DSA). Due to the photodiode's predominant responsivity from 850 nm to 1200 nm, we confined the SC real-time analysis within this spectral range while pumping the PCF fiber at 980 nm. The DSF fiber dispersion and slope are $\beta_2 = 3 \times 10^{-26} \text{ s}^2/\text{m}$ and $\beta_3 = 1 \times 10^{-39} \text{ s}^3/\text{m}$, respectively.

C.1. DFT experimental setup and measurements

To calibrate the DFT technique, it is essential to compare the spectral measurements obtained from the OSA with those from DFT measurements. For this purpose, we set up the configuration shown in figure 4 using both the OSA and DFT. The selection of the DSF for stretching the pulse must carefully consider the overlap length, determined by the DSF length and the dispersion coefficient β_2 . If the value of β_2 is too low, it may cause pulse overlap during numerical processing. In the case under study, we analyze a sequence of 400 pulses, each with a duration of 12.5 ns. Given the photodiode's bandwidth (B) of 25 MHz, we can determine the spectral resolution of the DFT-obtained spectra using the relation in equation 4 [21].

$$\delta\lambda = \frac{1}{B|D|z} \quad (4)$$

This relationship, which connects the dispersion value D to the pump wavelength and the fiber length L , allows us to calculate the spectral resolution as $\delta\lambda = 5$ nm. This resolution is crucial for evaluating the accuracy of our DFT measurements and ensuring they align as closely as possible with those taken using the OSA.

As shown in the bottom of Fig. 9, the spectrum obtained by the OSA (green curve) corresponds closely to the averaged spectrum measured by the DFT technique (red curve), although with a lower dynamics. Additionally,

the individual traces captured by the DFT (gray curves) reveal that the DW around $\lambda = 1150$ nm is generated with stable intensity across each pulse. In contrast, at $\lambda = 1050$ nm, the spectrum shows significant variations in intensity across individual traces. For the individual traces captured by the oscilloscope, this results in a strong variation in intensity in regions where the photodiode detection rate is weak, compared to areas with a higher capture rate.

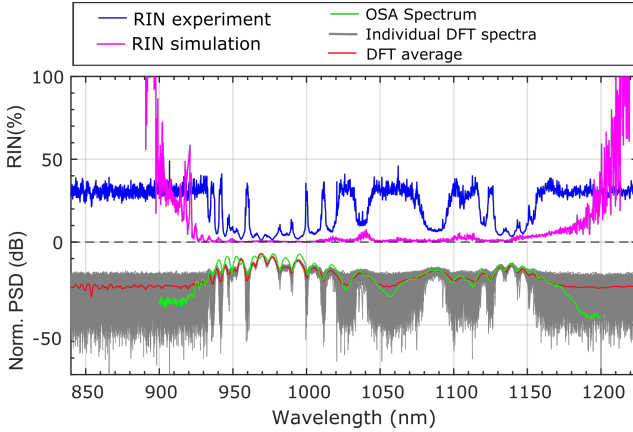


Fig. 9. Experimental results of the DFT study at $\lambda = 1000$ nm and $P = 7$ kW. Top : RIN measurements and simulations. Bottom: DFT and OSA measurements.

The DFT technique enables a detailed statistical analysis of the SC spectra, particularly through the measurement of relative intensity noise (RIN), as defined by equation 5, where $\tilde{A}(\lambda)$ represents the amplitude of the field in the spectral domain [16]. To compare the measured RIN with a simulated RIN, it is essential to account for noise variances. This includes considering the intrinsic quantum noise inherent in any laser system (one photon per mode (OPPM) model), an assumed amplitude noise of 2% corresponding to the laser's amplitude noise, and a phase noise of 6.2×10^{-6} , which aligns with the integrated phase noise value based on the Gaussian phase noise variance bounds. The RIN is a crucial metric for evaluating the overall stability of the SC, as it is calculated as the ratio of the standard deviation of the SC ensemble to its mean, as detailed in the following equation [16]:

$$RIN(\lambda) = \sqrt{\langle (|\tilde{A}(\lambda)|^2 - \langle |\tilde{A}(\lambda)|^2 \rangle)^2 \rangle} / \langle |\tilde{A}(\lambda)|^2 \rangle \quad (5)$$

The results presented in Figure 9 compare the RIN calculated from DFT spectra measured using the DFT method (blue curve) with the RIN derived from a SC spectrum simulated using the GNLSE (pink curve). In both cases, the noise percentage across the spectrum is notably low, particularly at the highest intensity points. However, in the numerical simulation, the RIN remains consistently low throughout the whole spectrum, not just at the peak intensities. This discrepancy arises because, in

the DFT measurements, the signal exhibits greater intensity variation compared to the numerical simulation. The DFT-derived RIN is influenced by the photon detection rate of the photodiode, which is lower in regions where the individual trace shows significant variation. On the other hand, the simulated RIN remains stable across the spectrum, except in areas where the signal diminishes. Additionally, the RIN peaks observed between $\lambda = 940$ nm and $\lambda = 1030$ nm correspond to spectral oscillations detected by DFT, indicative of the SPM phenomenon. The simulated RIN reveals that DW generation near 1100 nm introduces minimal noise, preserving excellent SC stability, with fluctuations as low as just a few percent.

4. CONCLUSION

In this work, we provided an extensive numerical and experimental investigation into the generation of dispersive waves (DWs) in optical fibers under normal dispersion pumping. Unlike DWs emitted by solitons in the normal dispersion regime, DWs in such case are generated in the anomalous dispersion regime with a modified phase-matching condition including the pump frequency chirp. Initially, we numerically investigated the OWB phenomenon, examining how third-order dispersion breaks the temporal and spectral symmetry and generates DW. This analysis highlighted the significance of including high-order dispersion in accurately modeling OWB and DW generation. Our investigation into DW generation involved comparing a model for DW positioning in the SC spectrum, based on parameters such as pump wavelength and initial peak power.

Following the numerical study, we experimentally examined the fiber we had modeled to verify the simulated properties. Our experimental results demonstrated excellent agreement with the numerical predictions. Additionally, we investigated the impact of polarization on DW generation and performed a comparison of our experimental data with results obtained using a DFT technique. This comparison confirms the coherence of our supercontinuum and the generated DW, with good agreement between the experimental and theoretical results.

For future work, we propose improving theoretical prediction techniques for DWs by improving the accuracy of shock velocity measurements. This refinement could yield results that align more closely with simulations and experiments. Furthermore, the findings from our study on DW and supercontinuum generation could be extended to the development of new types of normal dispersion fibers or nonlinear photonic integrated circuits (PICs), potentially leading to low-noise supercontinuum sources and better pulse compression rates.

5. ACKNOWLEDGMENTS

This work has received funding from the European commission (VISUAL project No. 101135904), and from the

Conseil Régional de Bourgogne Franche-Comté. The author thank Dr Matteo Conforti from University of Lille for helpful discussions.

6. DISCLOSURES

The authors have no conflicts of interest to declare.

REFERENCES

1. R. R. Alfano, *The Supercontinuum Laser Source: The Ultimate White Light* (Springer, 2016).
2. T. Sylvestre, E. Genier, A. N. Ghosh, *et al.*, "Recent advances in supercontinuum generation in specialty optical fibers," *JOSA B* **38**, F90–F103 (2021).
3. J. M. Dudley and J. R. Taylor, *Supercontinuum generation in optical fibers* (Cambridge university press, 2010).
4. G. P. Agrawal, "Nonlinear fiber optics, fifth edition," in *Nonlinear Science at the Dawn of the 21st Century*, (Academic Press, Elsevier, 2013).
5. I. Cristiani, R. Tediosi, L. Tartara, and V. Degiorgio, "Dispersive wave generation by solitons in microstructured optical fibers," *Opt. Express* **12**, 124–135 (2004).
6. A. Mussot, M. Beaugeois, M. Bouazaoui, and T. Sylvestre, "Tailoring cw supercontinuum generation in microstructured fibers with two-zero dispersion wavelengths," *Opt. Express* **15**, 11553–11563 (2007).
7. S. Roy, S. K. Bhadra, and G. P. Agrawal, "Effects of higher-order dispersion on resonant dispersive waves emitted by solitons," *Opt. Lett.* **34**, 2072–2074 (2009).
8. K. Webb, Y. Xu, M. Erkintalo, and S. Murdoch, "Generalized dispersive wave emission in nonlinear fiber optics," *Opt. Lett.* **38**, 151–153 (2013).
9. M. Conforti and S. Trillo, "Dispersive wave emission from wave breaking," *Opt. Lett.* **38**, 3815–3818 (2013).
10. M. Conforti, F. Baronio, and S. Trillo, "Resonant radiation shed by dispersive shock waves," *Phys. Rev. A* **89**, 013807 (2014).
11. M. Conforti, S. Trillo, A. Mussot, and A. Kudlinski, "Parametric excitation of multiple resonant radiations from localized wavepackets," *Sci. Reports* **5**, 9433 (2015).
12. Q. Lin and G. P. Agrawal, "Raman response function for silica fibers," *Opt. letters* **31**, 3086–3088 (2006).
13. C. Finot, B. Kibler, L. Provost, and S. Wabnitz, "Beneficial impact of wave-breaking for coherent continuum formation in normally dispersive nonlinear fibers," *JOSA B* **25**, 1938–1948 (2008).
14. A. M. Heidt, "Pulse preserving flat-top supercontinuum generation in all-normal dispersion photonic crystal fibers," *JOSA B* **27**, 550–559 (2010).
15. A. M. Heidt, A. Hartung, G. W. Bosman, *et al.*, "Coherent octave spanning near-infrared and visible supercontinuum generation in all-normal dispersion photonic crystal fibers," *Opt. express* **19**, 3775–3787 (2011).
16. E. Genier, S. Grelet, R. D. Engelsholm, *et al.*, "Ultra-flat, low-noise, and linearly polarized fiber supercontinuum source covering 670–1390 nm," *Opt. Lett.* **46**, 1820–1823 (2021).
17. W. Tomlinson, R. H. Stolen, and A. M. Johnson, "Optical wave breaking of pulses in nonlinear optical fibers," *Opt. letters* **10**, 457–459 (1985).
18. J. E. Rothenberg and D. Grischkowsky, "Observation of the formation of an optical intensity shock and wave breaking in the nonlinear propagation of pulses in optical fibers," *Phys. review letters* **62**, 531 (1989).
19. D. Anderson, M. Desaix, M. Lisak, and M. L. Quiroga-Teixeiro, "Wave breaking in nonlinear-optical fibers," *JOSA B* **9**, 1358–1361 (1992).
20. J. M. Dudley, L. P. Barry, P. G. Bollond, *et al.*, "Direct measurement of pulse distortion near the zero-dispersion wavelength in an optical fiber by frequency-resolved optical gating," *Opt. Lett.* **22**, 457–459 (1997).
21. S. Rao DS, T. Karpate, A. Nath Ghosh, *et al.*, "Noise in supercontinuum generated using pm and non-pm tellurite glass all-normal dispersion fibers," *Opt. Lett.* **47**, 2550–2553 (2022).
22. T. Godin, B. Wetzel, T. Sylvestre, *et al.*, "Real time noise and wavelength correlations in octave-spanning supercontinuum generation," *Opt. Express* **21**, 18452–18460 (2013).